Modeling and Control of a Variable-Length AUV

Rob McEwen
Monterey Bay Aquarium Research Institute
7700 Sandholdt Road
Moss Landing, CA 95039-9644
rob@mbari.org

Knut Streitlien
Bluefin Robotics, Corp.
301 Massachusetts Avenue
Cambridge, MA 02139
knut@bluefinrobotics.com

Revision 2.0

December 8, 2006

Contents

List of Figures

Abstract

The Monterey Bay Aquarium Research Institute (MBARI) is currently developing an AUV that has exchangeable midbody sections. Changing the midbody may consequently change the vehicle length.

The vehicle is actuated by an articulated ring-wing and partially ducted thruster, which gives the vehicle nearly complete axial symmetry.

In this paper we review the non-linear equations of motion used to model the vehicle. We then linearize them and compare predicted performance against field-test data. We discuss control issues that arise in the design of a variable-length vehicle.

1 Introduction

The MBARI AUV must serve as a general science platform in the Monterey Bay, which requires frequent changing of instrument packages. It must also be capable of long range, under-ice missions in the Arctic, as part of the Atlantic Layer Tracking Experiment (ALTEX) [4]. These disparate requirements have given rise to a modular design of exchangeable body segments, making the vehicle relatively easy to reconfigure. The tail section is common to all configurations. It carries the basic navigation and control electronics, and the propulsion system. See Figure 1 for a photograph of the vehicle.

Rather than the standard cruciform fin arrangement, this vehicle has an articulated ring-wing control surface with a ducted propeller. The purpose of the ring-wing is to physically protect the propeller while taking partial advantage of ducted-thruster characteristics. With the exception of the vertically mounted RF/GPS antenna, the ring-wing gives the vehicle complete axial symmetry. Figure 2 shows the ring-wing and propeller.

The ring-wing and the thruster are mounted together in a double gimbal arrangement. Rudder and elevator control is actuated by two linear-displacement stepper motors. The range of travel is $\pm 15^\circ$.

The hull shape is derived from the Series 58 Model 4154 Gertler polynomial [7], with a length of 84 inches, and a diameter of 21 inches. The hull is then extended by adding 21 inch diameter cylindrical midsections at the point of maximum diameter.

A 1° class AHRS, a DVL, a GPS, and a depth sensor provide the basic navigation. The vehicle carries various other types of sonars, including an LBL and an altimeter. For the ALTEX mission, the vehicle will carry a ring-laser gyro-based heading reference, and possibly a full INS system. The DVL will point upward to track off the ice.

Figure 1: 556 cm AUV With Two Midbodies

Figure 2: Ring-Wing and Propeller. Here there is only one 66 inch fuelcell midbody, and a 10 inch midbody for extra flotation, making the vehicle 419 cm in length. The vertical fin is the RF/GPS antenna.

2 Model of System Dynamics

2.1 Coordinate Systems and Notation

This report generally follows the SNAME [16] conventions for notation. We will take the origin of the vehicle-fixed reference frame to be at the mipoint of the vehicle. This implies that neither the center of mass nor the center of buoyancy will be at the origin. The body-fixed $\hat{b}_1$ is ahead and $\hat{b}_3$ is down.

The position of the vehicle will be referred to an Earth-fixed reference frame, with $\hat{n}_1$ pointing north, and $\hat{n}_3$ down. For the purposes of controls analysis, we will assume the Earth-fixed frame is inertially fixed. This frame will be referred to as N. Also, we'll assume that the fluid through which the vehicle travels is at rest with respect to the inertial frame. See [5], p. 6 for a diagram.

The symbols for translational and rotational velocities are $\vec{v}$ and $\vec{\omega}$, respectively. These will assume subscripts and superscripts. For example, ${}^{N}\vec{v}_{B}^{B_\circ}$ is the velocity of the origin of the body-fixed frame, $B_\circ$, with respect to the inertial frame N, coordinatized in the body-fixed frame, B. In the common case where the velocity is with respect to N, and is coordinatized in B, these two will be dropped to reduce clutter. Thus:

$$ {}^{N}\vec{v}_{B}^{B_\circ} \triangleq \vec{v}^{\,B_\circ} \triangleq \begin{bmatrix} u \\ v \\ w \end{bmatrix} \tag{1} $$

$$ \vec{\omega}^{\,B} \triangleq \begin{bmatrix} p \\ q \\ r \end{bmatrix} \tag{2} $$

The symbol for displacement is $\vec{r}$. Then, $\vec{r}^{\,N_\circ B_\circ}$ is the vector from the origin of the inertial frame to the origin of the body frame;

$$ \vec{r}^{\,N_\circ B_\circ} = \begin{bmatrix} x \\ y \\ z \end{bmatrix}_N \tag{3} $$

In general, a capital subscript on a vector specifies the frame in which the vector is coordinatized, as demonstrated in Equation 3.

Stability derivatives are denoted by the usual (X, Y, Z, K, M, N) with subscripts indicating the variables of differentiation. See [6] for a complete list of symbols. All stability derivatives are in dimensional form here.

2.2 Force Model for the Ring Control Surface

For the purposes of analysis, we will assume that the ring lift and drag vectors act at the ring center, which lies along the vehicle centerline. These vectors lie in the plane defined by the velocity of the water at the ring center, and the ring axis. Let $\vec{v}^{\,R_\circ}$ be the velocity of the ring center, $R_\circ$, with respect to an inertial frame (the water), N, coordinatized in the body-fixed frame, B. We can then define a Lift-Drag frame, LD, whose origin is fixed at the ring center, and whose x axis lies along $\vec{v}^{\,R_\circ}$. The perpendicular y axis lies in the plane defined by the ring axis and $\vec{v}^{\,R_\circ}$. See Figure 3 for a diagram of the ring frame.

Neglecting transient flow effects, the lift and drag of the ring are given by [13]:

$$L = \frac{1}{2}\rho A U^2 C_L(\alpha) \tag{4}$$

$$D = \frac{1}{2}\rho A U^2 C_D(\alpha) \tag{5}$$

where

$$C_L(\alpha) = C_{L\alpha}\alpha + C_{Dc}\alpha|\alpha| \tag{6}$$

$$C_D(\alpha) = C_{Do} + \frac{C_L(\alpha)^2}{\pi A_R e} \tag{7}$$

A_R is the aspect ratio, and A is the area of the ring defined as diameter $\times$ chord. The force applied to the body by the ring, coordinatized in the LD frame, is

$$\vec{F}_{LD} = \begin{bmatrix} -D \\ L \\ 0 \end{bmatrix}_{LD} \tag{8}$$

Now, consider a reference frame fixed in the ring, R, that is coincident with the vehicle body frame, B, when the rudder and elevator angles, δ_R and δ_E are zero. The direction cosine matrix that transforms a vector from B to R is

$$T_{R/B} = \begin{bmatrix} \cos\delta_R\cos\delta_E & \sin\delta_R & -\cos\delta_R\sin\delta_E \\ -\sin\delta_R\cos\delta_E & \cos\delta_R & \sin\delta_R\sin\delta_E \\ \sin\delta_E & 0 & \cos\delta_E \end{bmatrix} \tag{9}$$

The velocity of the ring center, $R_\circ$, in the ring frame is

$$\vec{v}_R^{\,R_\circ} = T_{R/B}\,\vec{v}^{\,R_\circ} \tag{10}$$

The direction cosine matrix that transforms a vector from LD to R can be determined by first setting

$$\vec{t}_1 = \vec{v}_R^{\,R_\circ} \tag{11}$$

$$\vec{t}_3 = \begin{bmatrix} 1 \\ 0 \\ 0 \end{bmatrix} \times \vec{v}_R^{R_\circ} \tag{12}$$

$$\vec{t}_2 = \vec{t}_3 \times \vec{t}_1 \tag{13}$$

Then,

$$T_{R/LD} = \begin{bmatrix} \hat{t}_1 & \hat{t}_2 & \hat{t}_3 \end{bmatrix} \tag{14}$$

where

$$\hat{t}_i = \frac{\vec{t}_i}{|\vec{t}_i|} \tag{15}$$

Figure 3 shows that the angle of attack is given by the following.

$$\alpha = \arcsin \frac{|\vec{v}_R^{R_\circ} \times \vec{r}_1|}{|\vec{v}_R^{R_\circ}|} \tag{16}$$

Finally, we can compute

$$\vec{F}_B = T_{B/R} \; T_{R/LD} \; \vec{F}_{LD} \tag{17}$$

The numeric realization of Eqn. 15 must be done carefully to avoid a division by zero since $|\vec{t}_2|$ and $|\vec{t}_3|$ approach zero for steady straight and level flight.

The velocity $\vec{v}^{\,R_\circ}$ is obtained from the vehicle states by the kinematic relation for a point fixed on a moving rigid body:

$$\vec{v}^{\,R_\circ} = \vec{v}^{\,B_\circ} + \vec{\omega}^{\,B} \times \vec{r}^{\,B_\circ R_\circ} \tag{18}$$

Our estimate for $dC_l/d\alpha = C_{L\alpha}$ for the ring wing shaped control surface is based on results from [14] (refering to work by [15]) and [3]. From Milewski's thesis [14]: $dC_l/d\alpha = 3.4855$ for $A_R = 1.25$, and the DSRV report [3] we have $dC_l/d\alpha = 5.1566$ for $A_R = 4.3716$. ($dC_l/d\alpha$ is slope of lift coefficient based on chord x diameter (α in radians), and A_R is aspect ratio, diameter/chord). Between these two points we would like to interpolate with a function of the form seen in van Dykes equation N.31 [18]:

$$\frac{dC_l}{\mathrm{d}\alpha} = \frac{2\pi}{1 + \frac{2}{A_R} + \frac{16}{\pi A_R^2} \log(1 + \pi e^{-9/8} A_R)}$$

This is an empirical expression for lift coefficient slope for elliptical wings of different aspect ratios, defined as planform area over maximum chord squared. We adopt this function to fit

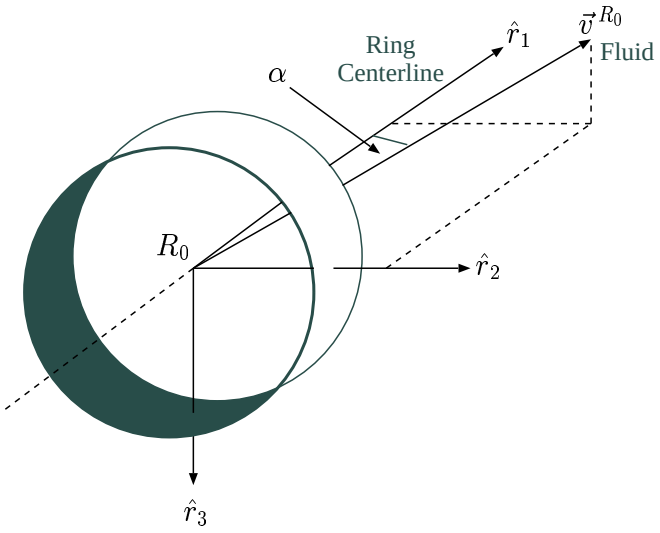

Figure 3: Coordinate Frame Definitions for the Ring

the ring wing results by allowing multiplicative parameters, r and s, in the definition of lift coefficient and aspect ratio:

$$\frac{dC_l}{\mathrm{d}\alpha} = \frac{2\pi r}{1 + \frac{2}{sA_R} + \frac{16}{\pi(sA_R)^2}\log(1 + \pi e^{-9/8} sA_R)} \tag{19}$$

Solving this nonlinear system results in

$$\begin{aligned} 2\pi r &= 5.9273 \\ s &= 4.305 \end{aligned}$$

Figure 4 shows Equation 19 passing through the two data points. Also shown is slope for lift coefficient based on duct frontal area, which is convenient for determining chord length for a fixed diameter. In our case then the ring aspect ratio is 3, which yields $dC_l/d\alpha = 4.8$.

2.3 Propulsion Model

The propulsion is modeled simply as a gimbaled thrust that acts at $R_\circ$, where T_p denotes thrust, not torque.

$$\left(\vec{F}_p\right)_B = T_{B/R} \begin{bmatrix} T_p \\ 0 \\ 0 \end{bmatrix} \tag{20}$$

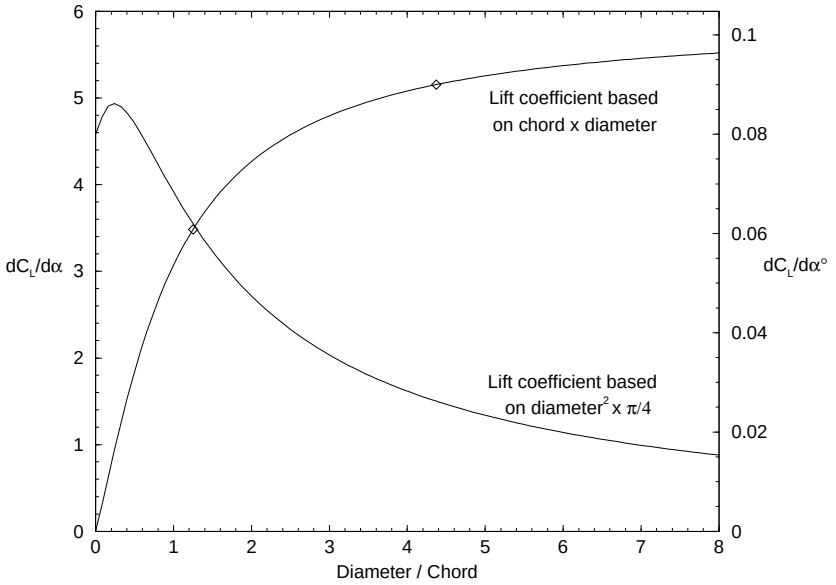

Figure 4: Lift coefficient slope for different aspect ratio ducts, based on two data points (diamonds). Between these, a function of the same form seen for elliptical planar wings has been assumed. The other graph shows the same result, but with lift coefficient defined on frontal area. The right hand ordinate axis shows indicates the slopes based on degrees, instead of radians.

$$= \quad T_p \begin{bmatrix} \cos\delta_E \cos\delta_R \\ \sin\delta_R \\ -\cos\delta_R \sin\delta_E \end{bmatrix} \tag{21}$$

Equation 9 has been substituted into 20 to get 21.

The ring center is on the vehicle centerline at distance x_R from the origin of the body-fixed axes,

$$\vec{r}^{\,B_\circ R_\circ} = \begin{bmatrix} x_R \\ 0 \\ 0 \end{bmatrix}_B \tag{22}$$

For this vehicle $x_R < 0$.

Reaction torque from the propeller is neglected in this analysis because the ring stators have been designed with a twist or "pre-swirl" such that they generate a roll torque that opposes and balances the reaction torque at all speeds.

2.4 Equations of Motion

The Equations of Motion (EOM) for this vehicle are based on the general case reported by Gertler and Hagen in [6]. They have also been derived in [11].

Force or torque terms that are negligible or do not apply have been dropped. These include terms related to a sail and a bowplane. The control and propulsion force and torque terms in [6] have been replaced with those derived above for this specific case. Thus, forces from the ring-wing control surface are not subsumed in the stability derivatives but are added explicitly.

The Deep Submergence Rescue Vehicle has a similar shape and is actuated by a ring-wing. See [3] for a thorough discussion of the EOMs.

All stability derivatives are in dimensional form here.

The effect of the RF/GPS antenna is neglected in the equations below.

T_p is the propulsion thrust along the ring centerline. (F_x, F_y, F_z) are the cartesian components of the lift and drag force generated by the ring, F_B, as derived in Section 2.2.

The EOM's are given as follows:

Surge Force

$$\begin{aligned} & m\left[\dot{u} - vr + wq - x_G(q^2 + r^2) + y_G(pq - \dot{r}) + z_G(pr + \dot{q})\right] \\ & \quad = X_{\dot{u}}\dot{u} \\ & \quad + X_{qq}q^2 + X_{rr}r^2 + X_{uu}u^2 + X_{vv}v^2 + X_{ww}w^2 + X_{vr}vr + X_{wq}wq \\ & \quad - (W - B)\sin\theta + T_p\cos\delta_R\cos\delta_E + F_x \end{aligned} \tag{23}$$

Sway Force

$$\begin{aligned} & m\left[\dot{v} - wp + ur - y_G(p^2 + r^2) + z_G(pr - \dot{p}) + x_G(qp + \dot{r})\right] \\ & \quad = Y_{\dot{r}}\dot{r} + Y_{\dot{p}}\dot{p} + Y_{\dot{v}}\dot{v} \\ & \quad + Y_{wp}wp + Y_r urY_v uv \\ & \quad + Y_{v|r|}v|r| + Y_{v|v|}v|v| + Y_{r|r|}r|r| + \\ & \quad (W - B)\cos\theta\sin\phi + T_p\sin\delta_R + F_y \end{aligned} \tag{24}$$

The original equations had a dependence on w in the $Y_{v|r|}\ v|r|$ and $Y_{v|v|}\ v|v|$ terms, which has been dropped. $Y_{r|r|}\ r|r|$ has been added.

Heave Force

$$\begin{aligned} & m\left[\dot{w} - uq + vp - z_G(p^2+q^2) + x_G(pr-\dot{q}) + y_G(rq+\dot{p})\right] \\ & \quad = Z_{\dot{q}}\dot{q} + Z_{\dot{w}}\dot{w} \\ & \quad + Z_{vp}vp + Z_q uq + Z_w uw \\ & \quad + Z_{w|w|}w|w| + Z_{q|q|}q|q| \\ & \quad + (W-B)\cos\theta\cos\phi - T_p\cos\delta_R\sin\delta_E + F_z \end{aligned} \tag{25}$$

The original equations had a dependence on v in the $Z_{w|w|}w|w|$ term, which has been dropped. $Z_{q|q|}q|q|$ has been added.

Roll Moment

$$\begin{aligned} & I_x\dot{p} + (I_z - I_y)qr - (\dot{r}+pq)I_{xz} + (r^2-q^2)I_{yz} + (pr-\dot{q})I_{xy} \\ & + m\left[y_G(\dot{w} - uq + vp) - z_G(\dot{v} - wp + ur)\right] \\ & \quad = K_{\dot{p}}\dot{p} + K_{\dot{v}}\dot{v} \\ & \quad + K_{p|p|}p|p| \\ & \quad + (y_G W - y_B B)\cos\theta\cos\phi - (z_G W - z_B B)\cos\theta\sin\phi \end{aligned} \tag{26}$$

The forces from the thruster and the ring lift and drag are considered to be bound at the ring center, which lies on the vehicle centerline. Thus neither can exert a roll moment, and the roll equation above is unforced.

Pitch Moment

$$\begin{aligned} & I_y\dot{q} + (I_x - I_z)rp - (\dot{q}+qr)I_{xy} + (p^2-r^2)I_{zx} + (qp-\dot{r})I_{yz} \\ & + m\left[z_G(\dot{u} - vr + wq) - x_G(\dot{w} - uq + vp)\right] \\ & \quad = M_{\dot{q}}\dot{q} + M_{\dot{w}}\dot{w} \\ & \quad + M_q uq + M_w uw + M_{rp}rp \\ & \quad + M_{q|q|}q|q| + M_{w|w|}w|w| \\ & \quad - (x_G W - x_B B)\cos\theta\cos\phi - (z_G W - z_B B)\sin\theta \\ & \quad - x_R(F_z + T_p\cos\delta_R\sin\delta_E) \end{aligned} \tag{27}$$

Yaw Moment

$$
\begin{aligned}
&I_z\dot{r} + (I_y - I_x)pq - (\dot{q} + rp)I_{yz} + (q^2 - p^2)I_{xy} + (rq - \dot{p})I_{zx} \\
&+m\left[x_G(\dot{v} - wp + ur) - y_G(\dot{u} - vr + wq)\right] \\
&\quad = N_{\dot{r}}\dot{r} + N_{\dot{v}}\dot{v} \\
&\quad +N_r ur + N_v uv + N_{pq}pq \\
&\quad +N_{r|r|}r|r| + N_{v|v|}v|v| \\
&\quad -(x_G W - x_B B)\cos\theta\sin\phi + (y_G W - y_B B)\sin\theta \\
&\quad +x_R(F_y + T_p \sin\delta_R)
\end{aligned} \tag{28}
$$

The kinematic equations are the standard 3-2-1 Euler sequence, and the associated derivatives. See [5], Eqn. 2.11, 2.14 and 2.15, for example.

Numerical values for the stability derivatives, mass properties, and other parameters above are included in Appendix A for the 556 cm vehicle. These have been analytically derived for this Gertler shape as functions of midbody length. See [17].

2.5 Determination of Center of Buoyancy and Center of Mass

The Center of Buoyancy (CB) and Center of Gravity (CG) locations discussed below include the water entrained in the hull.

We will assume that the drain and fastener holes in the hull are small enough to prevent significant a flow-through of water during nominal flight. Archimedes first principle then guarantees that the center of buoyancy will be at the volumetric center of the hull. Since our hull has axial symmetry, the center of buoyancy must lie along $\hat{b}_1$, which is the center line. Thus

$$y_B = z_B = 0 \tag{29}$$

We will additionally make the idealizing assumption that the entrained water remains motionless with respect to the body-fixed axes during flight.

It is impractical to analytically determine the location of the center-of-mass including the entrained water, so we have developed an experimental procedure to measure it. This involves hanging small weights from the vehicle, when its in the water, and using the AHRS to measure various steady-state roll angles.

2.6 Linearized Equations of Motion

Equations 23 through 28 have been linearized previously [10]. In this report we will linearize about the solution for steady straight-and-level flight at a constant speed U. In this section, the state u is considered to be a small perturbation about U. Likewise, the Euler angles (ϕ, θ, ψ) are considered to be small perturbations about equilibrium values, which are denoted by an overbar. The assumptions for linearity are then:

$$u, v, w \ll U \tag{30}$$
$$p \ll U/D \tag{31}$$
$$q, r \ll U/L \tag{32}$$
$$\phi, \theta \ll 1 \quad \text{radian} \tag{33}$$
$$\dot{T}_p,\ \dot{U} = 0 \tag{34}$$

L and D are the length and diameter, respectively, of the vehicle.

The linearized equations are of order 12. The following additional assumptions will cause the linearized equations decouple into a 4th order sway/yaw set, a 4th order heave/pitch set, and two decoupled 2nd order equations for axial translation, and roll.

$$\bar{\phi} = 0 \tag{35}$$
$$x_G \approx x_B \tag{36}$$
$$y_G \approx y_B \tag{37}$$
$$W \approx B \tag{38}$$

This decoupling is advantageous for controller design since the problem is reduced to two independent 4th order systems. However, the design should be checked for robustness against the full order linear model (excluding uncontrollable states) to evaluate the effect of coupling when Eqn. 35-38 aren't satisfied. Of primary concern is $\bar{\phi}$, which is the equilibrium roll angle. It sometimes has a nonnegligible value due to uncertainties inherent in the placement of ballast.

In certain cases, such as a transect between two waypoints, we will additionally assume $\bar{\psi} = 0$. The interpretation here is that the inertial frame N is displaced $\bar{\psi}$ from North, and then the body frame B remains within small angles of N. The state x is then considered to be down-range distance, and y is cross-track error.

Sway/Yaw

$$\begin{bmatrix} m - Y_{\dot{v}} & mx_G - Y_{\dot{r}} & 0 & 0 \\ mx_G - N_{\dot{v}} & I_{zz} - N_{\dot{r}} & 0 & 0 \\ 0 & 0 & 1 & 0 \\ 0 & 0 & 0 & 1 \end{bmatrix} \begin{bmatrix} \dot{v} \\ \dot{r} \\ \dot{y} \\ \dot{\psi} \end{bmatrix}$$

$$= \begin{bmatrix} (Y_v - Y_{RF} - Y_A)U & (Y_r - m - x_R Y_{RF} - x_A Y_A)U & 0 & 0 \\ (N_v - x_R Y_{RF} - x_A Y_A)U & (N_r - mx_G - x_R^2 Y_{RF} - x_A^2 Y_A)U & 0 & 0 \\ 0 & 1 & 0 & U \\ 0 & 0 & 0 & 1 \end{bmatrix} \begin{bmatrix} v \\ r \\ y \\ \psi \end{bmatrix}$$

$$+ \begin{bmatrix} Y_R U^2 + T_P \\ (Y_R U^2 + T_P) x_R \\ 0 \\ 0 \end{bmatrix} \delta_R \tag{39}$$

Y_{RF} is the sway force coefficient due to the rudder fixed in the neutral position,

$$Y_{RF} = \frac{1}{2}\rho A(C_{L\alpha} + C_{Do}) + \frac{1}{2}\rho A_S(C_{SL\alpha} + C_{SDo}) \tag{40}$$

A is the area of the ring, defined as chord $\times$ diameter. A_S is the equivalent strut area, defined to be $A_S = 2(1 + \sqrt{2}) \times$ (span) $\times$ (chord).

Y_A is the sway force due to the RF/GPS antenna fin;

$$Y_A = \frac{1}{2}\rho A_F(C_{FL\alpha} + C_{FDo}) \tag{41}$$

A_F is the area of the RF/GPS antenna. Y_R is the sway force coefficient due to a deflected rudder;

$$Y_R = \frac{1}{2}\rho A C_{L\alpha} \tag{42}$$

Heave/Pitch

$$\begin{bmatrix} m - Z_{\dot{w}} & -mx_G - Z_{\dot{q}} & 0 & 0 \\ -mx_G - M_{\dot{w}} & I_{yy} - M_{\dot{q}} & 0 & 0 \\ 0 & 0 & 1 & 0 \\ 0 & 0 & 0 & 1 \end{bmatrix} \begin{bmatrix} \dot{w} \\ \dot{q} \\ \dot{z} \\ \dot{\theta} \end{bmatrix}$$

$$= \begin{bmatrix} (Z_w - Z_{RF})U & (Z_q + m + x_R Z_{RF})U & 0 & 0 \\ (M_w + x_R Z_{RF})U & (M_q - mx_G - x_R^2 Z_{RF})U & 0 & W(z_B - z_G) \\ 1 & 0 & 0 & -U \\ 0 & 1 & 0 & 0 \end{bmatrix} \begin{bmatrix} w \\ q \\ z \\ \theta \end{bmatrix}$$

$$+ \begin{bmatrix} -(Z_R U^2 + T_P) \\ (Z_R U^2 + T_P) x_R \\ 0 \\ 0 \end{bmatrix} \delta_E \tag{43}$$

Due to symmetry we have

$$Z_w = Y_v \tag{44}$$
$$Z_q = -Y_r \tag{45}$$
$$M_w = -N_v \tag{46}$$
$$N_r = M_q \tag{47}$$
$$Z_R = Y_R \tag{48}$$
$$Z_{RF} = Y_{RF} \tag{49}$$

3 Control System

The analysis in this section is based on the linearized Equations 39-43. We will consider three vehicle lengths below: $L = (246, 389, 556)$ cm, corresponding to none, one or two midbodies, respectively.

3.1 Control Surface Design Considerations

An interesting property of a long and slender hull with a pointed tail is that, without any control surface area aft of the CG, it is longitudinally unstable. The Sway/Yaw Equation 39 shows this when Y_R and Y_A are set to zero. A design issue is then to decide how much lift is required from the ring to obtain open loop stability for $246 < L < 556$ cm.

Figure 5 shows the two non-zero open-loop time constants of Eqn. 39 as a function of control surface area. The values used in this equation are furnished in Appendix A. For $L = 556$ cm, the control surface must be greater than 0.030 meters^2 for open-loop stability.

The ring area was chosen to be $A = 0.048$ meters^2. However, the stators also provide considerable lift. The time constants including the stators are the right-hand endpoints of the curves.

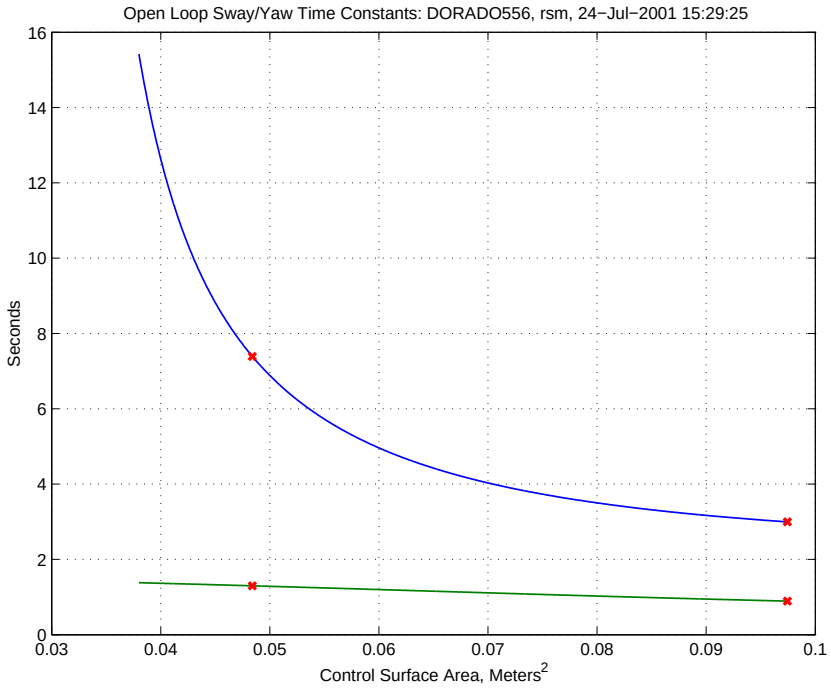

Figure 5: Stability Versus Ring Area for L = 556 cm

Another question that presents itself is "How is the stability affected by varying the length when the control surface area remains constant?" We can answer this since the mass properties and stability derivatives can be analytically parameterized by length, as shown in [17]. We will assume a representative value of $z_G = 6.5$ mm for all lengths. Figure 6 shows the open-loop Heave/Pitch time constants as a function of L. The vehicle response speeds up for shorter lengths. The Sway/Yaw EOM's show a similar trend.

3.2 Controllability

The roll dynamics have no control input and are consequently uncontrollable. Assuming that the thrust T_p and the speed U are constant, the longitudinal states $[\ u \quad x\ ]^T$ are likewise uncontrollable when evaluated against the full 12th order linearized model.

3.3 Sampling Rate Selection

The open-loop time constants (seconds) for the three lengths are:

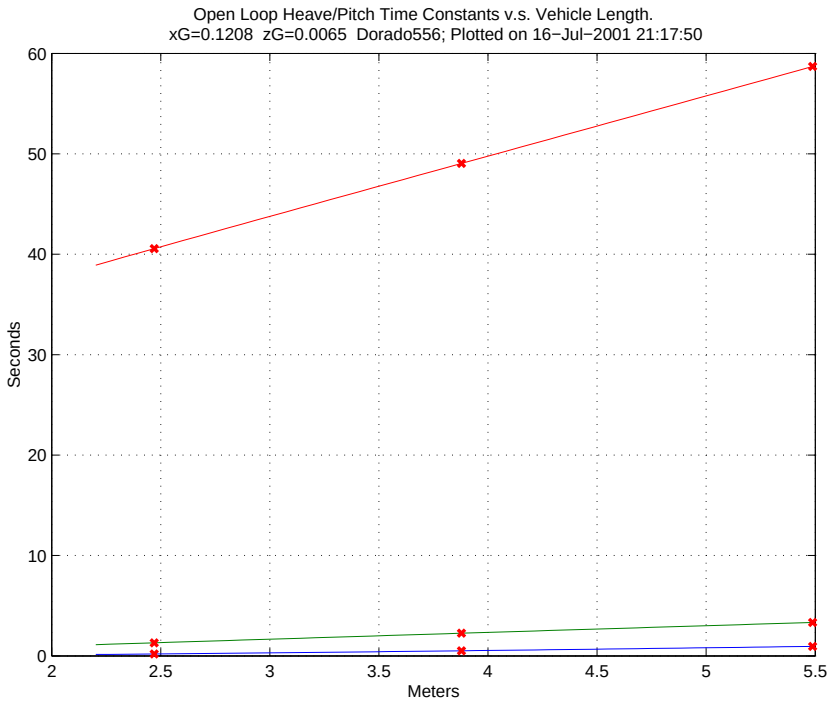

Figure 6: Stability Versus Length for Fixed Ring Area

246 cm	389 cm	556 cm
1.1787	2.0332	2.9586
0.1884	0.4812	0.8770
0.1933	0.5091	0.9475
1.3036	2.2575	3.3298
40.5611	49.0399	58.6956

This excludes poles at $s = 0$. The first two rows are the sway/yaw modes, and the others are heave/pitch.

We desire to control heading, cross-track error, pitch and depth (ϕ, y, θ, z). These all correspond to eigenvalues at zero, except depth which is the last row above. The other eigenvalues must remain stable and well damped in the closed-loop system. A sampling period of 0.2 seconds was selected.

3.4 Actuator Dynamics and Model

The rudder and elevator are actuated by two linear-displacement stepper motors that move a double gimbal. The outer gimbal is the elevator.

The stepper motors are rate-limited such that either gimbal can move no faster than 15 Degrees/second, or 0.042 Hz. Additionally, serial transmission delays of up to one second $(5T_s)$ occur routinely between the main vehicle computer and the motor control electronics.

Experience with the vehicle shows that the pitch control response is dominated by the stepper motor rate limit. We have consequently chosen to model this by a linear, second-order, critically-damped system with bandwidth 0.042 Hz.

3.5 Sway/Yaw and Heave/Pitch PID Control Loops

The control loop architecture currently in use is carried over from the Sea Grant Odyssey program. Figure 7 shows the Heave/Pitch control loop.

The outer loop is a Proportional-Integral control on depth error. Until recently, a direct measurement of depth rate has not been available, hence there is no rate term. The output of this controller is a commanded pitch angle, which serves as the setpoint for the pitch control. The pitch control is a PID. The gain values are selected such that the pitch loop has a bandwidth approximately ten times that of the outer depth loop.

An advantage of this arrangement is that the control can be easily switched into a pitch control mode, where the operators can explicitly specify a commanded pitch angle. This is accomplished by simply shutting off the outer depth loop.

Figure 8 shows the Sway/Yaw control loop, which is frequently operated in a heading-control mode where ψ_R is the commanded heading deviation, and K_{wp} is zero. Typically states v and y are not sensed or fed back.

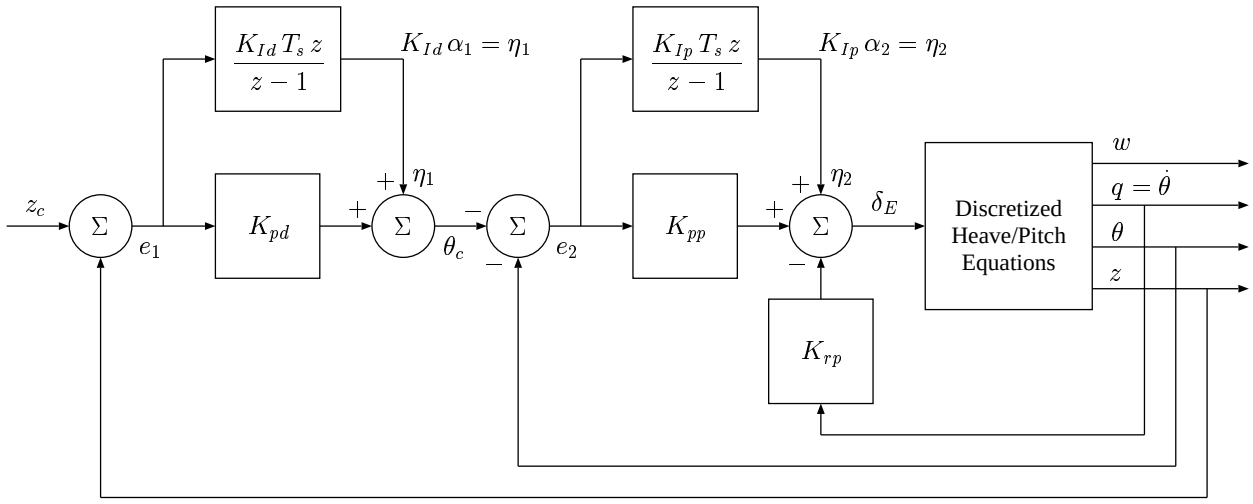

Figure 7: Heave/Pitch Control Loop

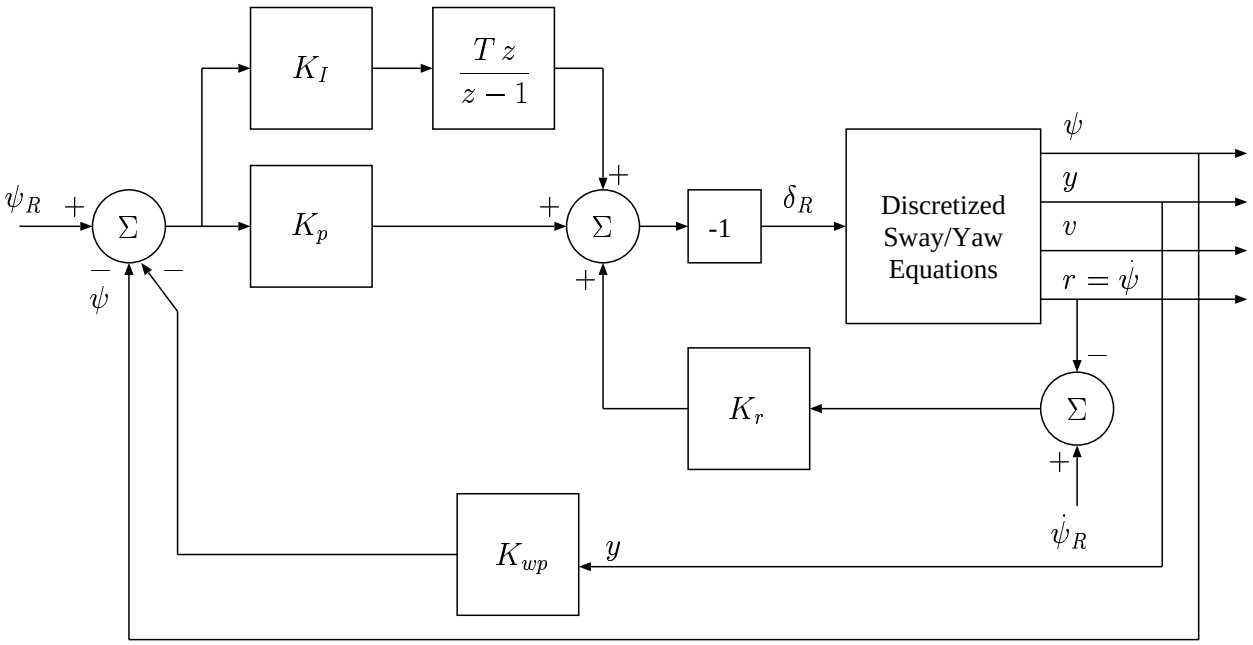

Figure 8: Sway/Yaw Control Loop

The loop may also be operated in a waypoint mode, where ψ_R is now interpreted as a commanded bearing deviation. The state y is estimated.

In the case of waypoints it is useful to consider vehicle motion relative to a rotated inertial frame where the $\hat{n}_1$ axis points in the direction of travel, as mentioned in Section 2.6. Thus ψ_R is always zero for nominal operation.

The interpretation of what the integrator now does is interesting. The integrator causes the following relation to be satisfied in the steady-state, where the ss subscript signifies steady-state.

$$\psi_{Rss} = \psi_{ss} + K_{wp} y_{ss} = 0 \tag{50}$$

The ψ_{ss} term denotes crab angle. The crab angle is typically due to a cross-current. Equation 50 then implies that the steady-state cross-track error is proportional to the crab angle. A typical value of K_{wp} is 0.05 meters^{-1}. Thus, if the crab angle is, say, 30°, the cross-track error will be 10.5 meters, assuming a steady cross-current. This may not be acceptable for certain applications such as sea-floor mapping.

Figure 9 shows an alternative control where the integrator is guaranteed to drive the cross-track error to zero. This is not yet implemented. The disadvantage of this is that for setpoint operation the integrator would have to be switched back as in Figure 8, which would lead to complications involving initializing the integrator state whenever the mode is switched. Also, this implementation is not effective until the navigation error is less than y_{ss} (ten meters).

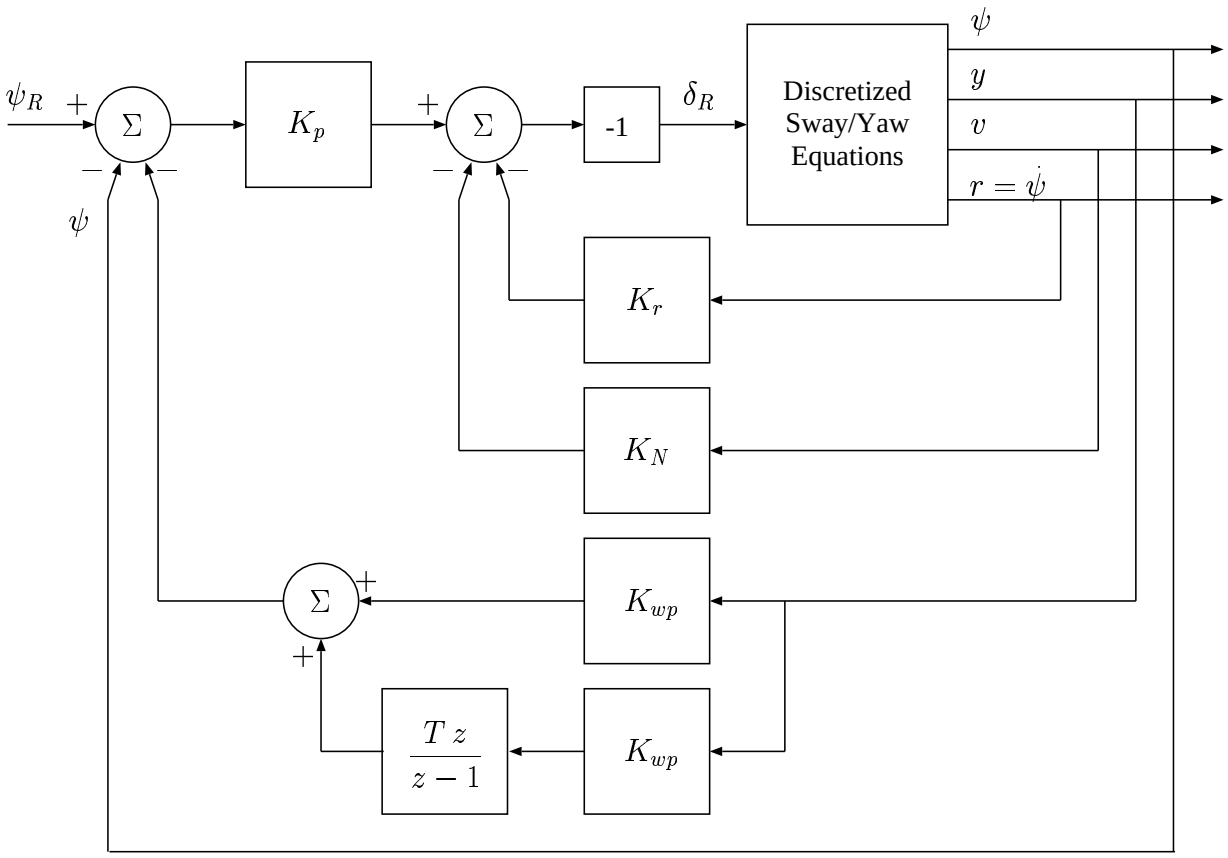

Figure 9: Modified Sway/Yaw Control Loop

3.6 Design Evaluation

We will concentrate on the Heave/Pitch dynamics of the 556 vehicle, as it is the most difficult to control.

Initial gain values have been chosen by trial and error for the PID architecture shown in Figures 7 and 8. See A.1 for the values for the 556 cm vehicle. Until recently, significant errors between the model and measured performance prevented an analytic design. Future work will include an analytic determination of gains based on the model, as well as more advanced control strategies.

The eigenvalues of the pitch control loop, excluding the depth loop, are:

```
Damping ratio, natural frequency (hz), time constant, 3*t.c.:

   2.5265e-01   5.2756e-02   1.1941e+01   3.5822e+01
   2.5265e-01   5.2756e-02   1.1941e+01   3.5822e+01

Time constant, 3 time constants (seconds):

            0            0
   8.4191e-01   2.5257e+00
   7.3640e+01   2.2092e+02
   3.1354e+00   9.4062e+00
   2.0999e+00   6.2996e+00
```

A step response shows that the actuator poles at 0.053 Hz dominate, which agrees with observation. The slow pole at 73.6 seconds is nearly canceled by a zero and does not appreciably affect the step response. The pitch control bandwidth is 0.07 Hz.

Closing the outer depth loop gives the following eigenvalues:

```
Damping ratio, natural frequency (hz), time constant, 3*t.c.:

   2.6585e-01   5.1628e-02   1.1596e+01   3.4787e+01
   2.6585e-01   5.1628e-02   1.1596e+01   3.4787e+01
   2.2982e-01   4.6371e-03   1.4934e+02   4.4803e+02
   2.2982e-01   4.6371e-03   1.4934e+02   4.4803e+02

Time constant, 3 time constants (seconds):

   8.4102e-01   2.5231e+00
   2.1050e+00   6.3151e+00
   3.3258e+00   9.9775e+00
   7.4755e+01   2.2426e+02
```

The pitch control eigenvalues have not changed much, but the response will now be dominated by much slower and lightly damped depth poles at 0.0046 Hz. The depth control closed loop bandwidth is 0.008 Hz, much slower than the inner pitch control loop.

Figure 10 shows the depth step response of the linear model. The second smoother curve is depth response without actuator dynamics. Since the depth loop is so much slower than pitch, the 0.042 Hz actuator mode in the pitch dynamics have little effect on the depth response.

Figure 11 shows the pitch angle, the elevator angle, and various other quantities. The 0.042 Hz actuator mode is apparent.

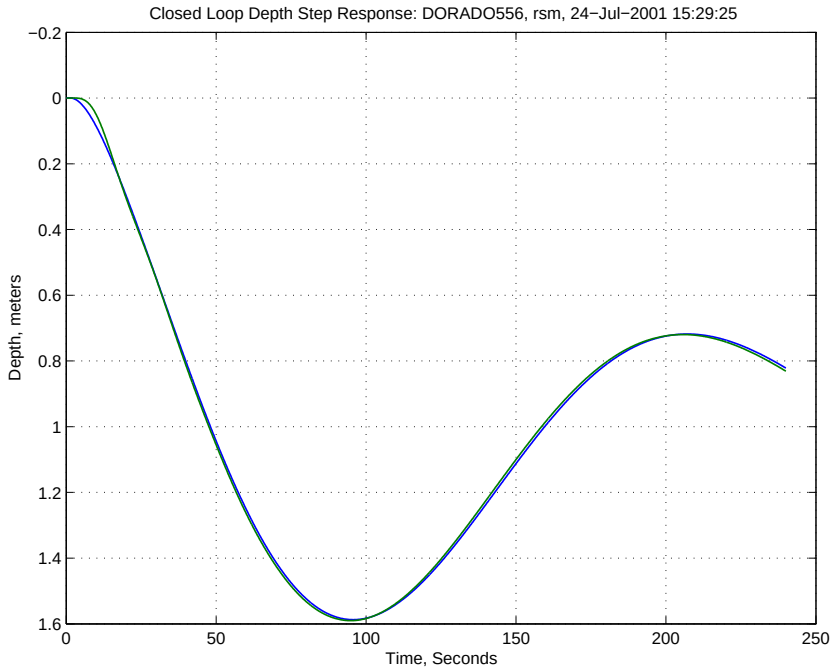

Figure 10: Depth Step Response of the Linearized Closed-Loop System

Since the actuator dynamics significantly degrade the pitch control, it seems prudent to check the robustness of the control loop at the actuator input. Figure 12 shows a root locus of the depth loop on actuator gain, where the loop is opened at the actuator input. The entire locus isn't shown.

Figure 12 is interesting in that it shows the depth poles (the inner locus) moving to the left, but the actuator poles moving to the right, as gain increases. This suggests that the system has an upper and lower gain margin. The margins are $+22/-17$ dB, and the phase margin is 105 Degrees.

Another area of concern is robustness with respect to CG shift. This is particularly important for the Altex mission because the fuel cell will both lose weight in expelled gas,

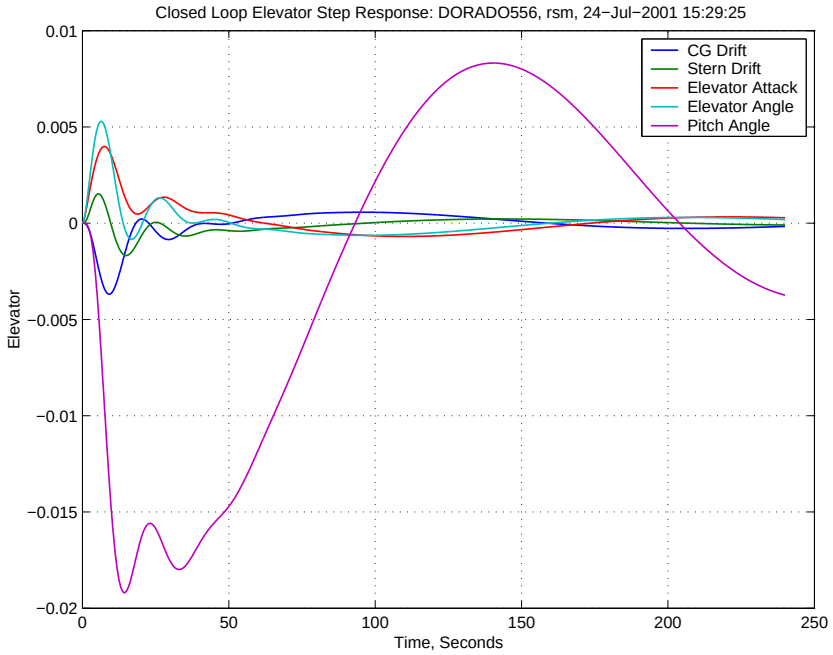

Figure 11: Pitch and Elevator Response of the Linearized Closed-Loop System for a Depth Step

and will shift it's CG lower as the aluminum anode plates oxidize and turn into precipitates.

Figure 13 shows a root locus of the closed loop system on the center of mass, z_G. The actuator poles move to the right, but the depth poles become unstable as $z_G \rightarrow 200$mm. We do not expect the CG to exceed 20mm during the course of the Altex mission, which is not enough to destabilize the loop. This will be verified in future tests.

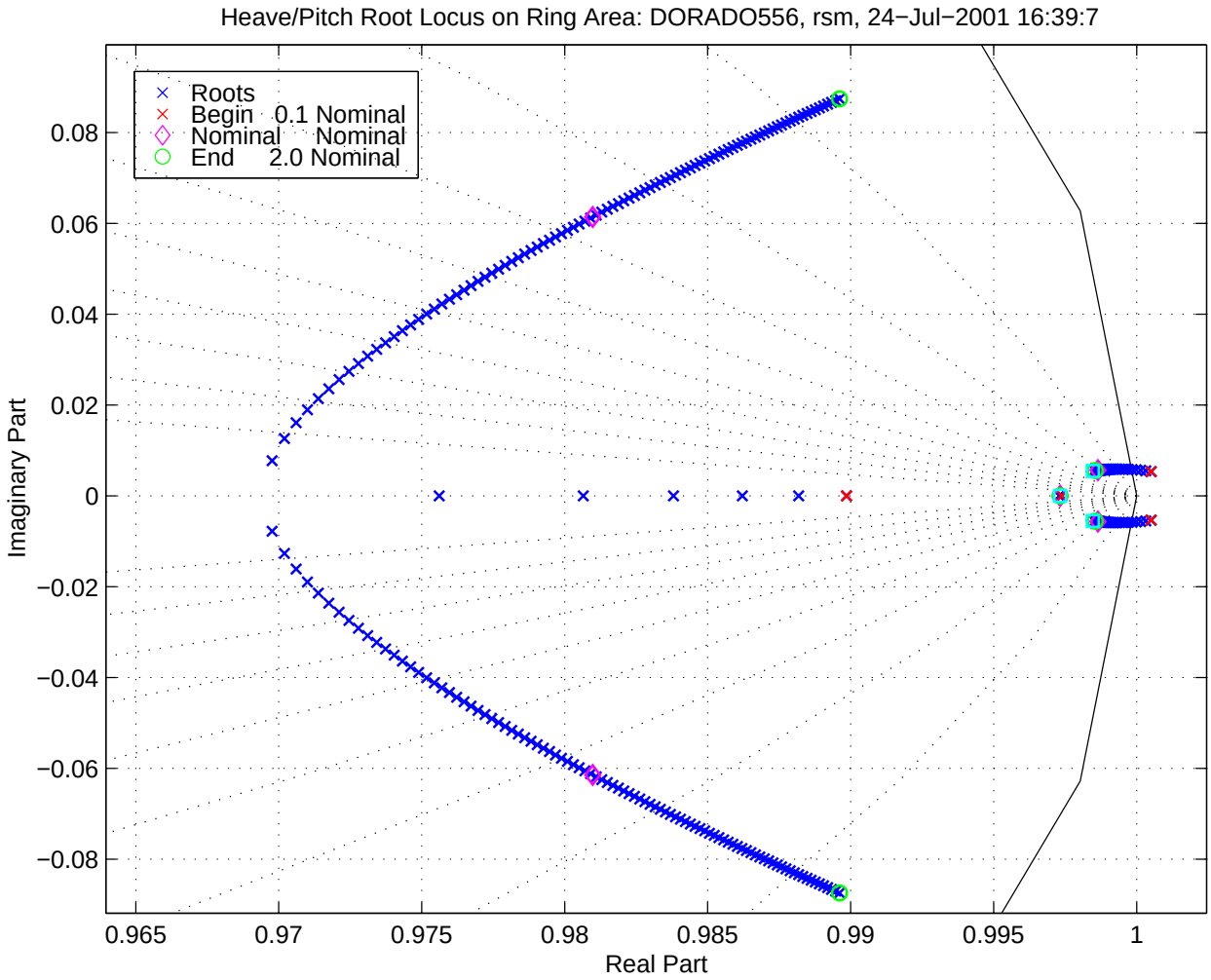

Figure 12: Partial Root Locus of the Depth Control System on Actuator Gain. This is equivalent to a locus on Ring Area.

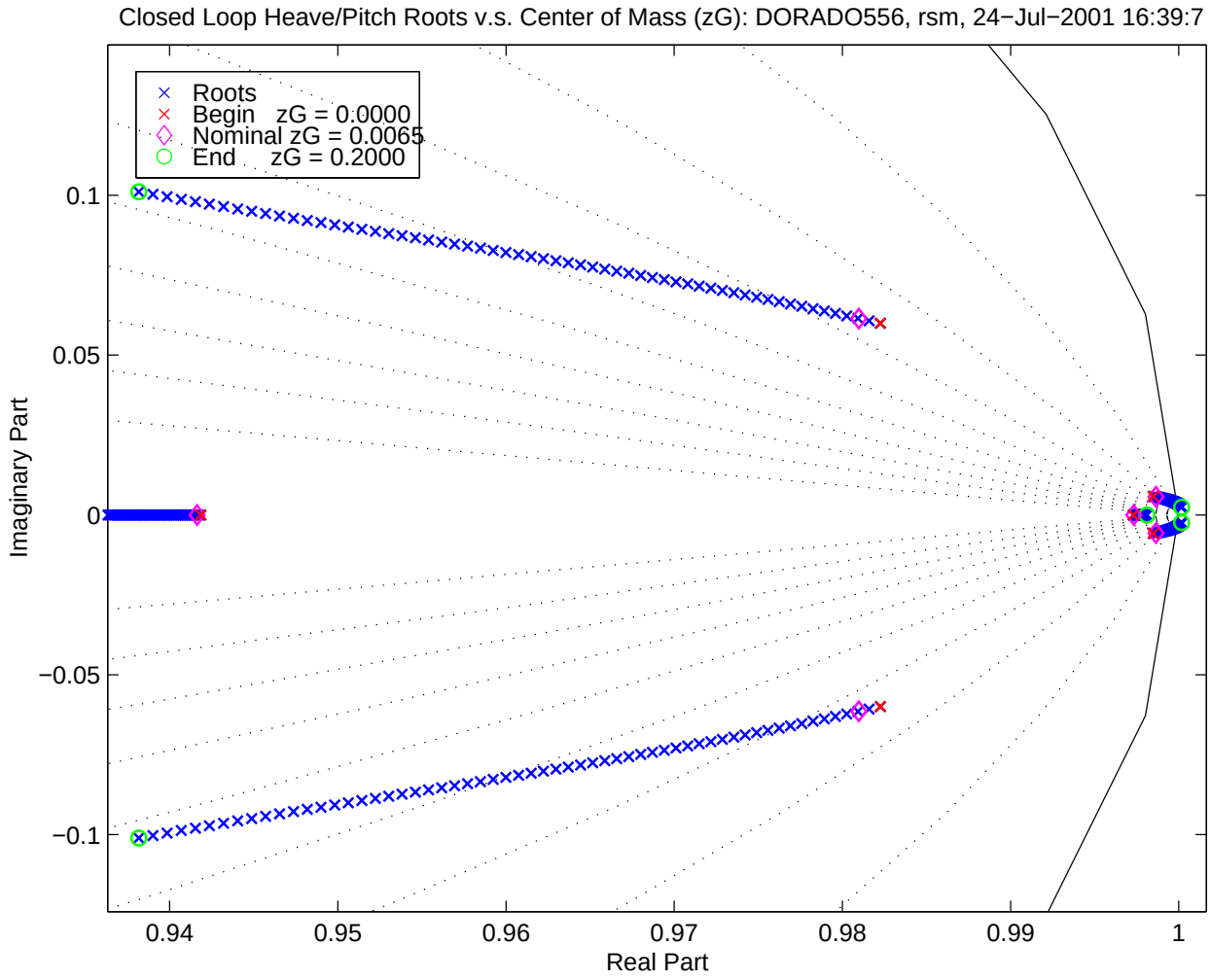

Figure 13: Partial Root Locus of the Depth Control System on Center-of-Mass

3.7 Model Validation and Identification: Comparison to Data

This section contains plots from a rudder step-response test for the 556 cm vehicle. The underdamped modes in depth and pitch described in the preceding sections are evident.

The test was a $\pm 10^\circ$ rudder deflection at a depth of 15 meters. Figure 14 shows the ground track of the vehicle. The fixed rudder causes the two opposing loops. The bottom strip of Figure 15 shows the commanded rudder angle. In between steps, the rudder was fixed at -2°, which is near neutral.

The effect on the depth control is visible in Figure 16. The upper strip shows depth, and the middle strip shows commanded and measured pitch. The vehicle displays a damped oscillation in depth. The measured depth descends past the commanded at 108 seconds, and again at 322, giving a period of 214. This compares well with the inverse of the damped natural frequency computed in Section 3.6, which is 221 seconds.

At 376 seconds the rudder steps to -10° which excites the actuator mode, which is modeled to have a period of 20.1 seconds. The pitch oscillation in the figure, beginning at 375 seconds, and again at 506 seconds, has a period of 21 seconds. Corresponding elevator oscillations are visible in the bottom strip.

The top strip of Figure 17 shows an equilibrium roll angle of -4.5°. The vehicle rolls to near zero when it makes its first turn to starboard, but then rolls to about -10° during the turn to port. There is concern that roll angles much larger than this will couple Sway/Yaw with Heave/Pitch.

The bottom strip of Figure 18 shows that the vehicle achieves approximately a $\pm 5^\circ$ turn rate for rudder deflections of 10°. The linear Sway/Yaw model in Equation 39 predicts 4.5°/second. The nonlinear terms may be significant at this turn rate.

Figure 19 shows the three components of velocity as measured by the DVL, that is, $\vec{v}^{DVL_\circ}$. The DVL is not located at the vehicle midpoint, but is just aft the RF/GPS antenna. See Figure 2. Substituting $\vec{r}^{\,B_\circ DVL_\circ}$ in Equation 18 instead of $\vec{r}^{\,B_\circ R_\circ}$, and using steady-state values from Equation 39 gives a predicted value of 0.37 meters/second. The measured value from the second strip is 0.40.

4 Conclusions and Future Work

We have described the equations of motion, both nonlinear and linear, for the MBARI AUV. Eigenvalues and linear step responses were computed and shown to be in reasonable agreement with measured data.

In evaluating the linear equations against the data, we found that the stepper motor rate limit caused significant oscillations in the pitch controller. The analytic models were brought into agreement with the data by including a second-order roll-off to model the rate limit.

Some exciting topics for future work are:

1. Modify the control architecture in Figures 7 and 8 to include full-state feedback. Investigate using the DVL to measure the three states u, v, w $(= \vec{v}^{\,B_\circ})$.

2. Derive an observer or possibly a Kalman filter to estimate biases and ocean currents. This estimator may also need to propagate $\vec{v}^{\,B_\circ}$ between updates as it is unlikely that the DVL will be able to sample at the control system rate of 5 Hz.

3. Investigate a low-power, cruise mode of control, which samples and actuates at a much lower rate.

4. Analyze vehicle performance at low-speeds and with a significant roll angle.

5. Analyze Heave/Pitch and Sway/Yaw coupling caused by the RF/GPS antenna. This and the preceding item require the full 12 state coupled linear equations.

References

[1] H. Julian Allen and Edward W. Perkins. Characteristics of flow over inclined bodies of revolution. Research Memorandum A50L07, NACA, 1951. Available on line, URL: http://naca.larc.nasa.gov/reports/1951/naca-rm-a50l07/.

[2] John D. Brooks and Thomas G. Lang. Simplified methods for estimating torpedo drag. In Leonard Greiner, editor, *Underwater Missile Propulsion*, pages 117–146. Compass Publiations, 1967.

[3] Charles Broxmeyer et al. Deep submergence rescue vehicle simulation and ship control analysis. Technical Report R-570-A, Instrumentation Laboratory, MIT, Cambridge, MA, Feb 1967.

[4] James G. Bellingham et al. An arctic basin obersvational capability using auvs. *Oceanography*, 13(2):64–70, 2000.

[5] Thor I. Fossen. *Guidance and Control of Ocean Vehicles*. Wiley & Sons, New York, 1994.

[6] M. Gertler and G. Hagen. Standard equations of motion for submarine simulation. Report 2510, David W. Taylor Naval Ship Research and Development Center, 1967.

[7] Morton Gertler. Resistance experiments on a systematic series of streamlined bodies of revolution – for application to the design of high-speed submarines. Report C-297, Navy Department, The David taylor Model Basin, Apr 1950.

[8] S.F. Hoerner. *Fluid Dynamic Drag*. Hoerner, Midland Park, NJ, 1958.

[9] Sighard .F. Hoerner and Henry V. Borst. *Fluid Dynamic Lift*. Hoerner Fluid Dynamics, Vancouver, WA, 1985.

[10] Franz Hover. Control system design for the odyssey II vehicle. MIT Sea Grant / WHOI, Oct 1995.

[11] Franz Hover. Physical modelling of the odyssey II vehicle. MIT Sea Grant / WHOI, Apr 1995.

[12] L. Landweber and J.L Johnson. Prediction of dynamic stability derivatives of an elongated. Report C-359, David Taylor Model Basin, Washington, D.C., 1951.

[13] Edward V. Lewis, editor. *Principles of Naval Architecture, Second Revision*. Society of Naval Architects and Marine Engineers, third edition, 1989.

[14] William Michael Milewski. *Three-dimensional viscous flow computations using the integral boundary layer equations simultaneously coupled with a low order panel method*. PhD thesis, Massachusetts Institute of Technology, Jun 1997.

[15] W.B. Morgan and E.B. Caster. Prediction of the aerodynamic characteristics of annular airfoils. Technical Report 1830, David Taylor Model Basin, 1965.

[16] SNAME. Nomenclature for treating the motion of a submerged body through a fluid. Technical and Research Bulletin 1-5, Society of Naval Arcitects and Marine Engineers, 1964.

[17] Knut Streitlien. Altex hydrodynamic coefficients revisited. MIT Sea Grant College Program, AUV Laboratory, July 2000.

[18] M. van Dyke. *Perturbation Methods in Fluid Mechanics*. The Parabolic Press, 1975.

[19] Frank M. White. *Viscous Fluid Flow*. McGraw-Hill, 1974.

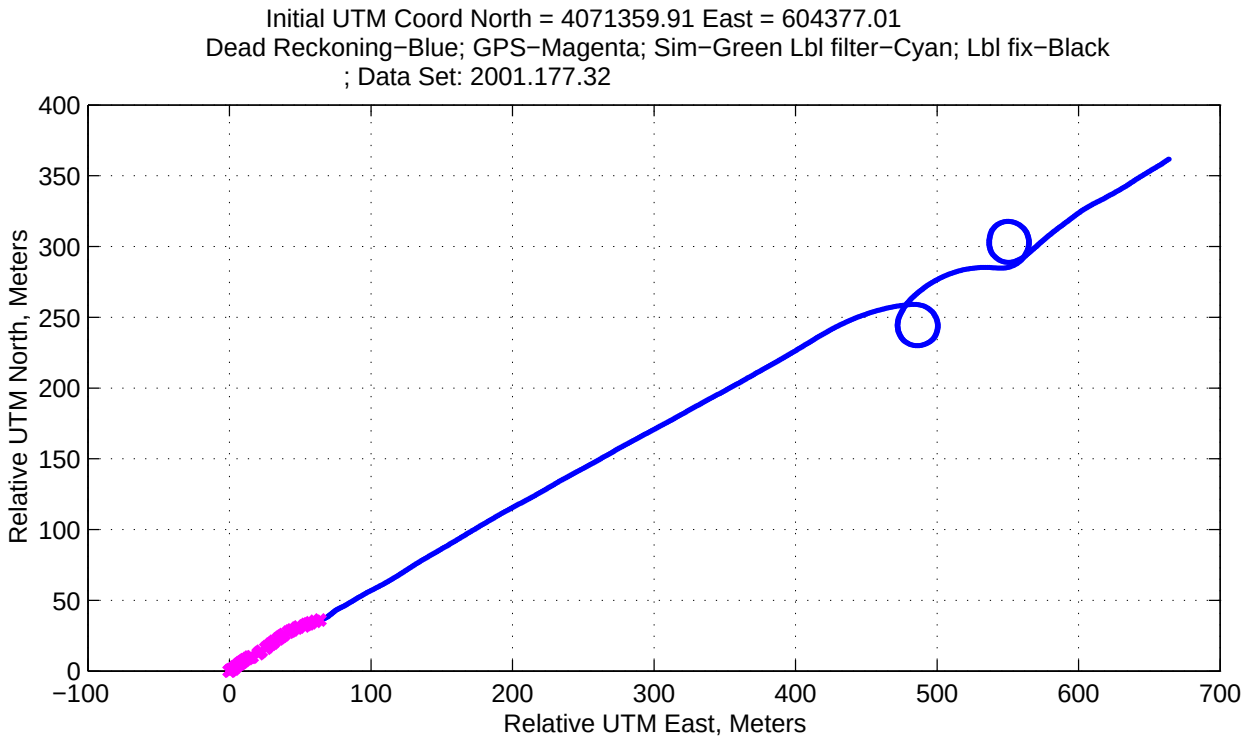

Figure 14: Ground Track

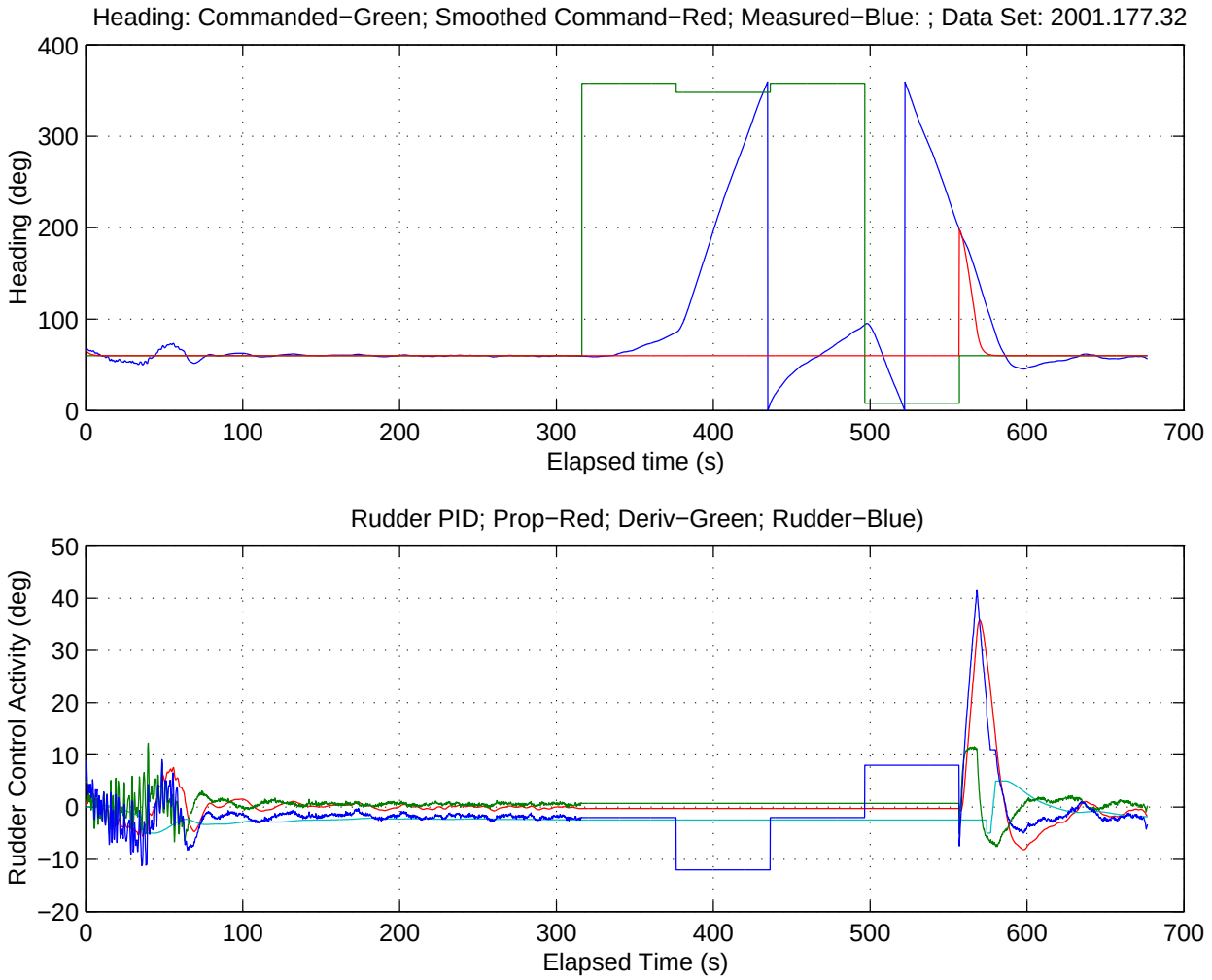

Figure 15: Heading and Rudder Angles

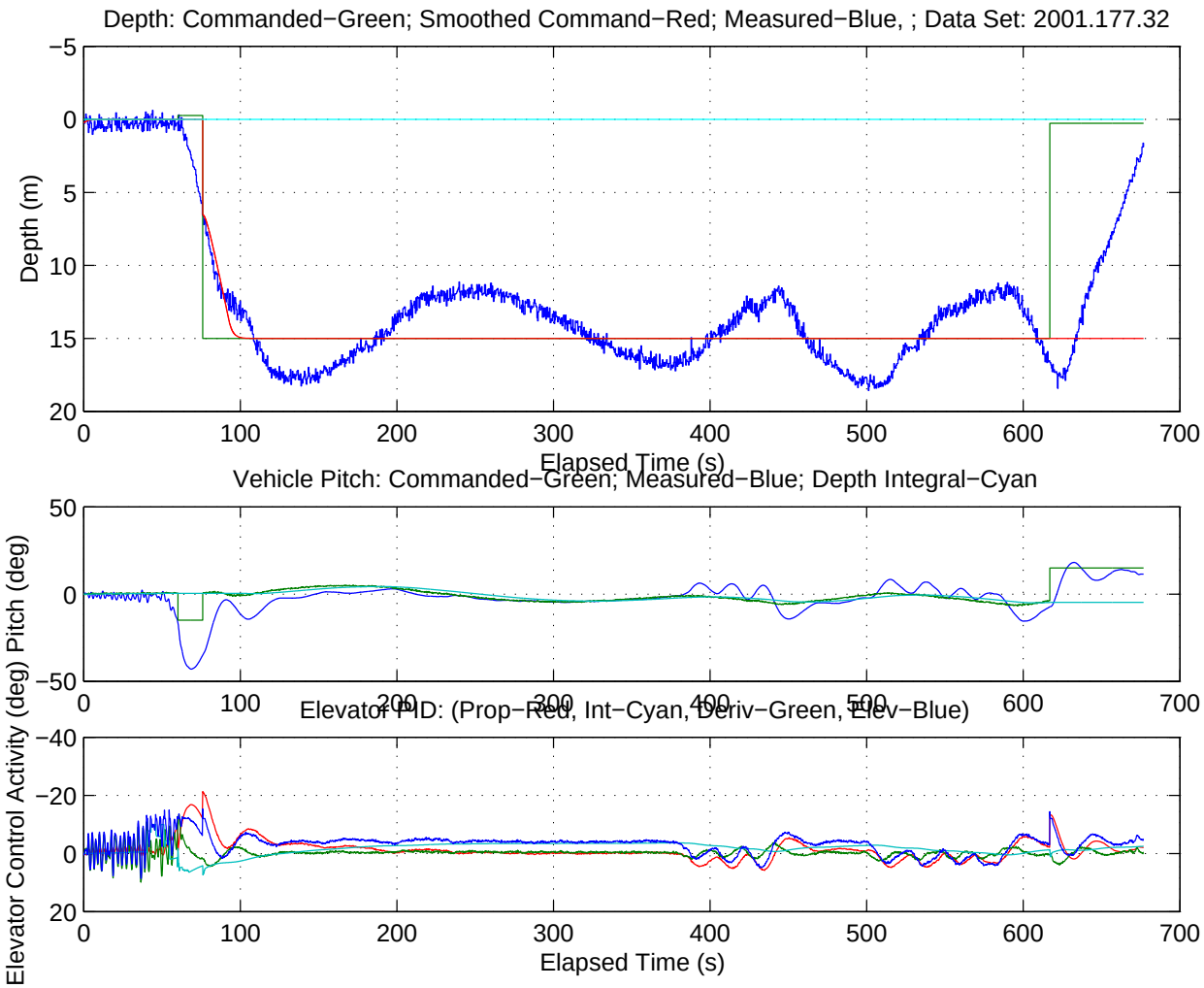

Figure 16: Depth, Pitch and Elevator Angles

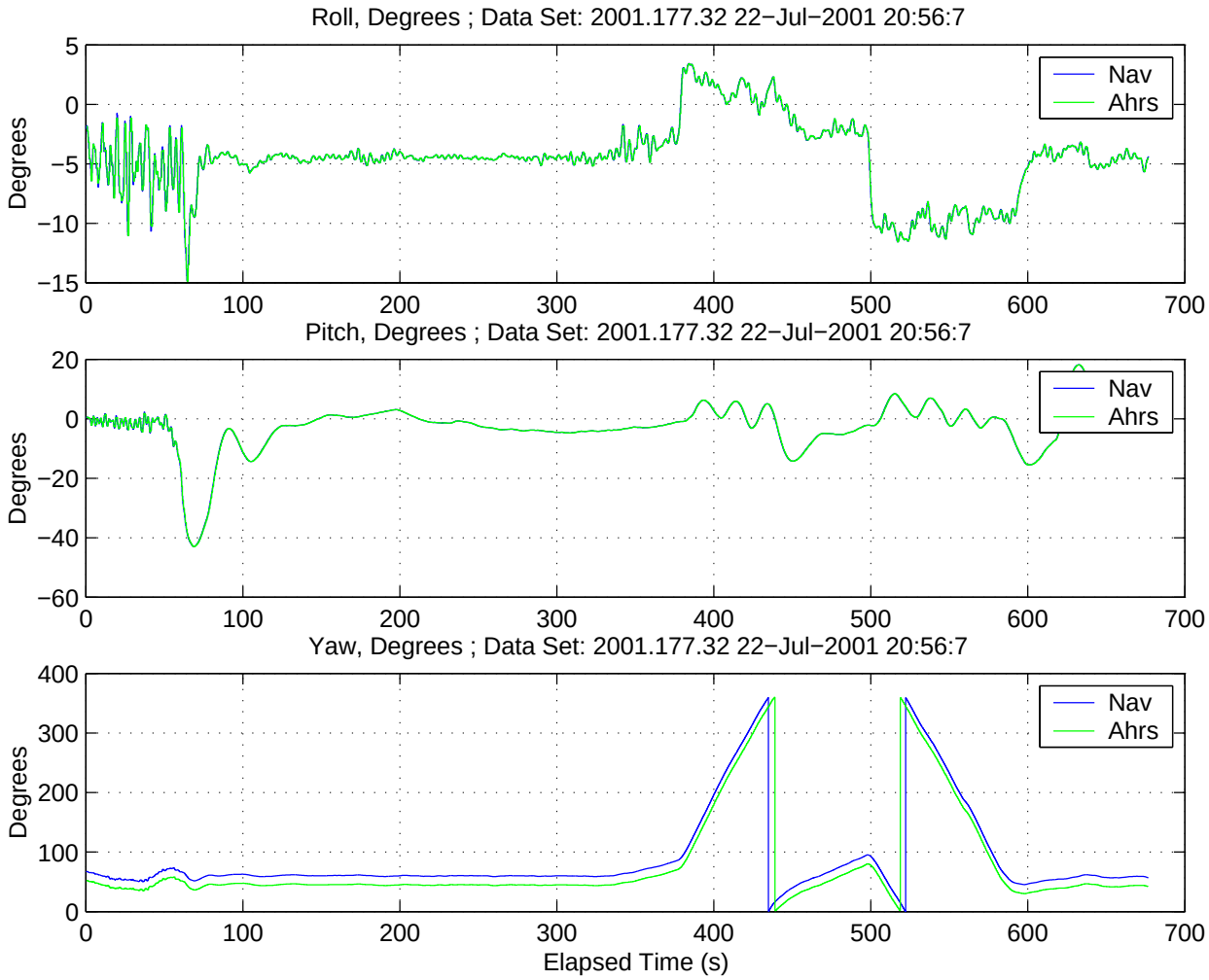

Figure 17: Roll, Pitch and Yaw Angles Measured by AHRS

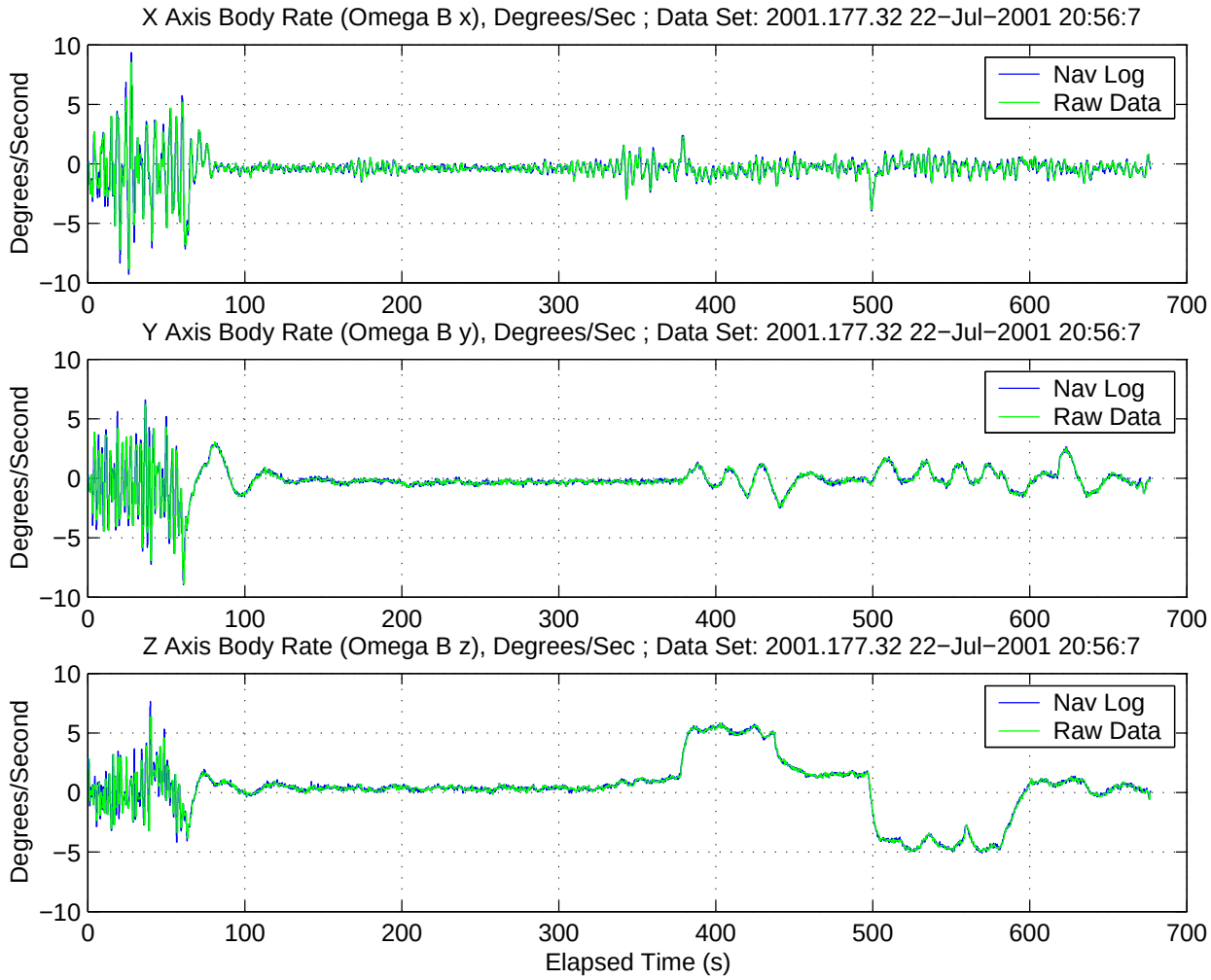

Figure 18: Body Rates Measured by AHRS

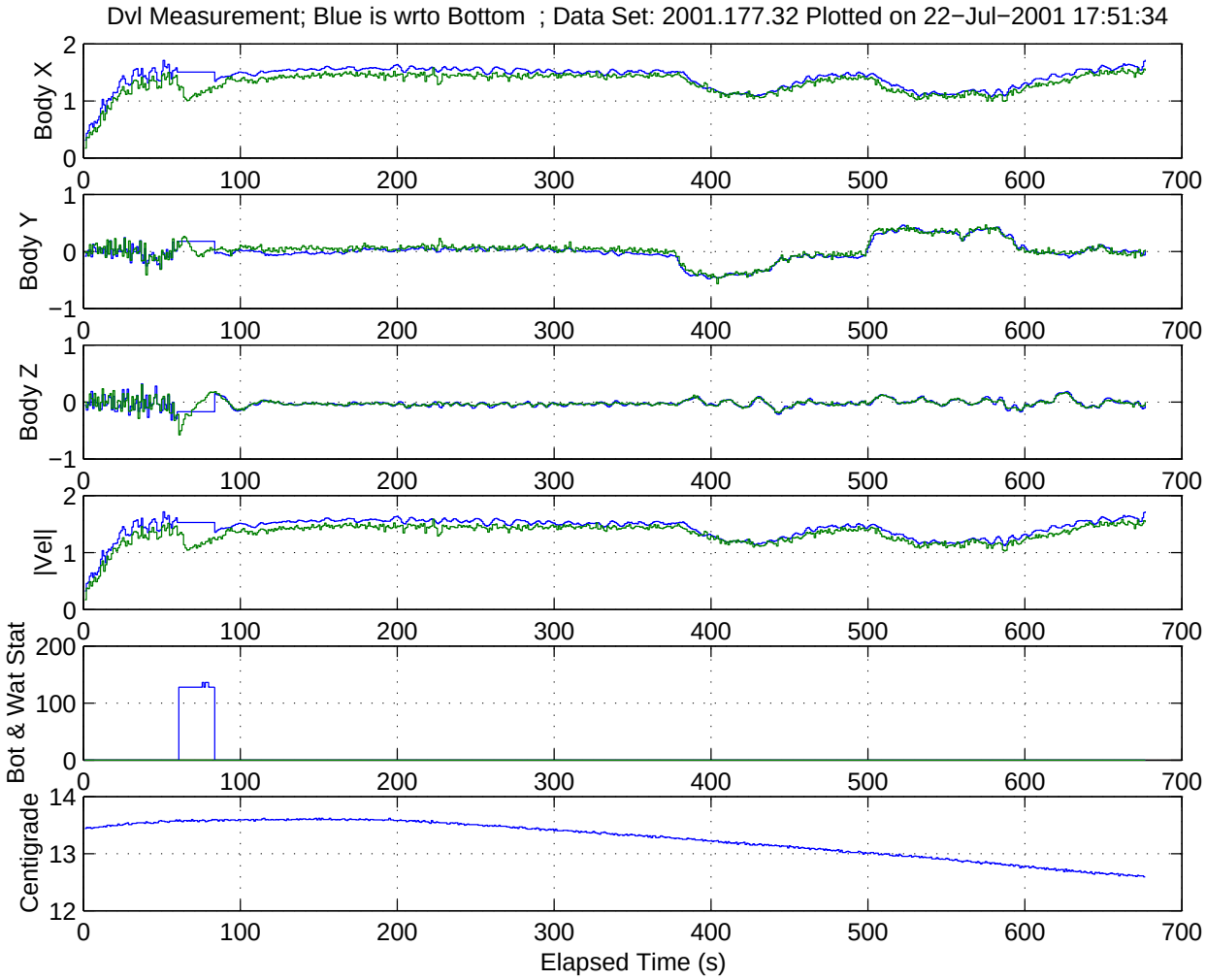

Figure 19: $\vec{v}^{DVLo}$ Measured by the DVL

A Numerical Values

A.1 Mass Properties and Stability Derivatives for Simulation

```
DORADO556 PARAMETERS

-- Mass Properties --
1089.814286    : (mass) Mass, kg.
2154.307591    : (Izz) Inertia about (principal) z axis, kg-m^2.
36.677779      : (Ixx) Inertia about (principal) x axis, kg-m^2.
5.554800       : (len) Length, Meters.
18.224409      : (len) Length, feet.
0.533400       : (dia) Diameter, Meters.
21.000000      : (dia) Diameter, Inches.
-2.777400      : (xR) Distance from CG to CP of ring, Meters.
-2.853600      : (xP) Distance from CG to pivot point, Meters.
0.120877       : (xG) x CG offset, Meters.
0.000000       : (yG) y CG offset, Meters.
0.006500       : (zG) z CG offset, Meters.
0.120877       : (xB) x CB offset, Meters.
0.000000       : (yB) y CB offset, Meters.
0.000000       : (zB) z CB offset, Meters.
-0.076200      : (xPcp) Dist from pivot to ring CP, Meters.
-3.000000      : (xPcp) Dist from pivot to ring CP, In.
0.063500       : (aR)  Dist from c.l. to rudder actuator base, m
0.063500       : (rR2) Dist from c.l. to rudder actuator pivot, m
0.025400       : (rR1) Body x Dist from Tailc. Pivot to Rudder Act. Pvt, m
-- Vehicle Control System --
0.200000       : (Ts) Control System Sampling Interval, Sec.
3.000000       : (vel) Forward speed, knots.
52.000000      : (Tp) Thrust, Newtons.
0.560000       : (Kph) Heading position gain, unitless.
1.600000       : (Krh) Heading rate gain, seconds.
0.000000       : (Kvh) Sway rate (v) gain, rad/(meters/sec).
0.016000       : (Kih) Original Heading integral gain, 1/sec.
0.000000       : (Kwp) Sway (Waypoint) gain, rad/meter.
0.000000       : (Kiwp)Sway (Waypoint) integral gain, rad/sec/m.
0.750000       : (Kpp) Pitch position gain, unitless.
1.500000       : (Krp) Pitch rate gain, seconds.
0.010000       : (Kip) Pitch integral gain, 1/sec.
0.011000       : (Kpd) Depth position gain, rad/meter.
0.000500       : (Kid) Depth integral gain, rad/meter/sec.
```

```
-- Tailcone --
15.000000      : (maxDeltaR) Max. Rudder Deflection, Deg.
2400.000000    : (maxActDisp) Max Act. Displacement, counts.
1200.000000    : (maxActRate) Max Actuator Displacement Rate, Counts/Sec
240.000000     : (maxActDispTs) Max Act. Displacement in one Ts, Counts/sample
1.150000       : (ampsAct) Actuator current, full on, amps.
-- Control Surface Hydrodynamic Properties --
0.129677       : (TotalArea) Area of ring and struts, M^2.
278.303019     : (YdeltaRFixed) Sway force due to fixed rudder.
277.751689     : (YdeltaR) Sway force coeff. due to rudder deflection.
   - Fins or Struts -
0.010161       : (StrutArea) Control surface Area, Meters^2.
15.750000      : (StrutArea) Control surface Area, Inches^2.
0.049063       : (LinCtrlArea) Equivalent control surface area, Meters^2.
76.047727      : (LinCtrlArea) Equivalent control surface area, Inches^2.
6.280000       : (dCl) Coeff. of lift slope.
0.810000       : (Cdc) Crossflow drag coefficient
0.012000       : (Cd0) Constant component of drag coeff.
3.111111       : (Ar) Ring/strut aspect ratio.
0.900000       : (Ef) Oswald efficiency factor.
   - Ring -
0.048387       : (RingArea) Control surface Area, Meters^2.
75.000000      : (RingArea) Control surface Area, Inches^2.
4.800000       : (dClR) Coeff. of lift slope.
0.810000       : (CdcR) Crossflow drag coefficient
0.010000       : (Cd0R) Constant component of drag coeff.
4.260000       : (ArR) Ring/strut aspect ratio.
0.900000       : (EfR) Oswald efficiency factor.
-- Fuselage Hydrodynamic Properties --
 - Added Mass -
Yvdot  =-1043.590806;  // Yvdot, kg.
Zwdot  =-1043.590806;  // Zwdot, kg.
Xudot  =  -26.209663;  // Xudot, kg.
Mqdot  =-1907.084102;  // Mqdot, kg-m^2.
Nrdot  =-1907.084102;  // Nrdot, kg-m^2.
Kpdot  =    0.000000;  // Kpdot, kg-m^2.
Kvdot  =    0.000000;  // Kvdot, kg-m.
Mwdot  =  114.059185;  // Mwdot, kg-m.
Zqdot  =  114.059185;  // Zqdot, kg-m.
Nvdot  = -114.059185;  // Nvdot, kg-m.
Yrdot  = -114.059185;  // Yrdot, kg-m.
Ypdot  =    0.000000;  // Ypdot, kg-m.
```

```
 - Stability Derivatives -
Kpabp  =   -0.311429;  // Kp|p| , kg-m^2
Nuv    = -885.121594;  // Nuv   , kg
Nur    = -490.416429;  // Nur   , kg-m
Xvv    =  -67.911429;  // Xvv   , kg/m
Xww    =  -67.911429;  // Xww   , kg/m
Xvr    = 1043.590806;  // Xvr   , kg
Xwq    =-1043.590806;  // Xwq   , kg
Xrr    =  114.059185;  // Xrr   , kg-m
Xqq    =  114.059185;  // Xqq   , kg-m
Yuv    = -138.000394;  // Yuv   , kg/m
Yur    =   82.771766;  // Yur   , kg
Nrabr  =-2850.198251;  // Nr|r| , kg-m^2
Mqabq  =-2850.198251;  // Mq|q| , kg-m^2
Nvabv  =  486.816877;  // Nv|v| , kg
Ywp    = 1043.590806;  // Ywp   , kg-m
Yrabr  =    0.000000;  // Yr|r| , ?
Yvabv  = -920.141796;  // Yv|v| , kg/m
Zwabw  = -920.141796;  // Zw|w| , kg/m
Mwabw  = -486.816877;  // Mw|w| , kg
Zqabq  =    0.000000;  // Zq|q| , ?
Muq    = -490.416429;  // Muq   , kg-m
Muw    =  885.121594;  // Muw   , kg
Mpr    = 1907.084102;  // Mpr   , kg-m^2
Npq    =-1907.084102;  // Npq   , kg-m^2
Zuq    =  -82.771766;  // Zuq   , kg
Zuw    = -138.000394;  // Zuw   , kg/m
Zvp    =-1043.590806;  // Zvp   , kg
```

A.2 Expanded List of Stability Derivatives

The table below shows all nonzero coefficients that are used in simulations. Inertal quantities are all found analytically from the shape of the body, assuming it is the same density as water. Some adjustments have been incorporated , since the entrained water is not likely to move as a rigid body. Added mass properties are found from analytical results for basic shapes such as spheroids, cylinders, and plates, combined with strip theory. Munk moment and viscous lift and drag force coefficients were collected from [12], [2], [1], [8], [9], [18], [19].

		Body	Propulsor	Appendages	Total
l	[m]:				5.554800
m	[kg]:	1089.814286	0.200000	3.100000	1093.114286

xCB	[m]:	0.120877	-1.877400	-2.777400	0.112961
zCB	[m]:			-0.391700	
Ix	[kg m^2]:				36.677779
Iy	[kg m^2]:				2154.307591
Iz	[kg m^2]:				2154.307591
Xudot	[kg]:	-26.209663	-0.400000	0.000000	-26.609663
Xvdot	[kg]:	0.000000	0.000000	0.000000	0.000000
Xwdot	[kg]:	0.000000	0.000000	0.000000	0.000000
Xpdot	[kg m]:	0.000000	0.000000	0.000000	0.000000
Xqdot	[kg m]:	0.000000	0.000000	0.000000	0.000000
Xrdot	[kg m]:	0.000000	0.000000	0.000000	0.000000
Yvdot	[kg]:	-1043.590806	-15.000000	-1.300000	-1059.890806
Ywdot	[kg]:	0.000000	0.000000	0.000000	0.000000
Yqdot	[kg m]:	0.000000	0.000000	0.000000	0.000000
Ypdot	[kg m]:	-0.520000	-0.520000	0.000000	0.000000
Zwdot	[kg]:	-1043.590806	-15.000000	0.000000	-1058.590806
Zpdot	[kg m]:	0.000000	0.000000	0.000000	0.000000
Zqdot	[kg m]:	71.457236	-2.440949	114.059185	-40.161000
Zrdot:	[kg m]:	0.000000	0.000000	0.000000	0.000000
Kpdot	[kg m^2]:	0.000000	-0.041040	-0.185000	-0.226040
Kqdot	[kg m^2]:	0.000000	0.000000	0.000000	0.000000
Krdot	[kg m^2]:	0.976380	0.976380	0.000000	0.000000
Mwdot	[kg m]:	73.898185	0.000000	114.059185	-40.161000
Mqdot	[kg m^2]:	-1907.084102	-107.527061	0.000000	-2014.611163
Mrdot	[kg m^2]:	0.000000	0.000000	0.000000	0.000000
Nrdot	[kg m^2]:	-1907.084102	-107.527061	-4.583255	-2019.194419
Ypdot,Kvdot	[kg m]:	0.000000	0.000000	-0.520000	0.000000
Nvdot,Yrdot	[kg m]:	-114.059185	40.161000	2.440949	-71.457236
Zqdot,Nwdot	[kg m]:	114.059185	-40.161000	-2.440949	71.457236
Npdot,Krdot	[kg m^2]:	0.000000	0.000000	0.976380	0.976380
Xuu	[kg/m]:	-25.502857	0.000000	2.000000	-23.502857
Xvv	[kg/m]:	-67.911429	-0.240000	-0.490000	-68.641429
Xww	[kg/m]:	-67.911429	0.000000	-0.490000	-68.401429
Xpr	[kg m]:	0.520000	0.520000	-0.000000	-0.000000
Xqw	[kg]:	-1058.590806	0.000000	-1043.590806	-15.000000
Xqq	[kg m]:	114.059185	0.000000	-3.779836	110.279349
Xrv	[kg]:	1059.890806	1.300000	1043.590806	15.000000
Xrr	[kg m]:	114.059185	0.450576	-3.779836	110.729925
Xdrdr	[kg/m]:			-0.490000	
Xdsds	[kg/m]:			-0.490000	
Yv	[kg/m]:	-138.000394	-40.750000	-190.540000	-369.290394
Yv|v|	[kg/m]:	-920.141796	0.000000	0.000000	-920.141796

```
Yp              [kg]:     0.000000   -15.961775     0.000000   -15.961775
Ypw           [kg m]:  1073.590806    15.000000  1043.590806    15.000000
Yp|p|         [kg m]:     0.000000     0.000000     0.000000     0.000000
Yqp        [kg m^2]:   -33.737185    40.161000  -114.059185    40.161000
Yr              [kg]:    82.771766    76.504050   529.205796   688.481612
Ydr           [kg/m]:                            190.540000
Zw            [kg/m]:  -138.000394     0.000000  -190.540000  -328.540394
Zw|w|         [kg/m]:  -920.141796     0.000000     0.000000  -920.141796
Zpv             [kg]: -1073.590806   -15.000000 -1043.590806   -15.000000
Zpp           [kg m]:     0.000000     0.000000     0.000000     0.000000
Zpr           [kg m]:   -33.737185    40.161000  -114.059185    40.161000
Zq              [kg]:   -82.771766     0.000000  -190.540000  -273.311766
Zds             [kg]:                            -190.540000
Kv              [kg]:     0.000000   -15.961775     0.000000   -15.961775
Kv|v|           [kg]:     0.000000     0.000000     0.000000     0.000000
Kvw             [kg]:     1.300000     1.300000     0.000000     0.000000
Kvq        [kg m s]:    -2.440949    -2.440949     0.000000     0.000000
Kwr             [kg]:     2.440949     2.440949     0.000000     0.000000
Kp            [kg m]:     0.000000    -7.150000    -2.960000   -10.110000
Kpw        [kg m s]:     0.520000     0.520000    -0.000000    -0.000000
Kp|p|      [kg m^2]:    -0.311429     0.000000     0.000000    -0.311429
Kqr        [kg m^2]: -4033.805582    -4.583255 -3814.168204  -215.054123
Kr            [kg m]:     0.000000    29.966636     0.000000    29.966636
Mw              [kg]:   885.121594     0.000000  -529.205796   355.915798
Mw|w|           [kg]:  -486.816877     0.000000     0.000000  -486.816877
Mpv        [kg m s]:    73.898185    -0.000000   114.059185   -40.161000
Mpr        [kg m^2]:  2019.112339     4.542215  1907.084102   107.486021
Mq            [kg m]:  -490.416429     0.000000  1469.816178   979.399749
Mq|q|      [kg m^2]: -2850.198251     0.000000     0.000000 -2850.198251
Mrv        [kg m s]:     0.520000     0.520000    -0.000000    -0.000000
Nv              [kg]:  -885.121594    76.504050   529.205796  -279.411748
Nvq           [kg m]:    -0.000000    -0.000000    -0.000000    -0.000000
Nv|v|           [kg]:   486.816877     0.000000     0.000000   486.816877
Nwp           [kg m]:    33.737185   -40.161000   114.059185   -40.161000
Np            [kg m]:     0.000000    29.966636     0.000000    29.966636
Np|p|      [kg m^2]:     0.000000     0.000000     0.000000     0.000000
Nqp        [kg m^2]: -2121.912185  -107.342061 -1907.084102  -107.486021
Nr            [kg m]:  -490.416429  -143.628703 -1469.816178 -2103.861310
Nr|r|      [kg m^2]: -2850.198251     0.000000     0.000000 -2850.198251
}
```